A hybrid metal artifact reduction algorithm for x-ray CT

Yanbo Zhang
Institute of Image Processing and Pattern Recognition, Xi'an Jiaotong University, Xi'an,
Shaanxi 710049, China

Hao Yan and Xun Jia
Center for Advanced Radiotherapy Technologies and Department of Radiation Medicine and Applied Sciences,
University of California San Diego, La Jolla, California 92037

Jian Yang
Department of Diagnostic Radiology, The First Hospital of Medical School, Xi'an Jiaotong University, Xi'an,
Shannxi Province 710061, China

Steve B. Jiang
Center for Advanced Radiotherapy Technologies and Department of Radiation Medicine and Applied Sciences,
University of California San Diego, La Jolla, California 92037

Xuanqin Mou[a)]
Institute of Image Processing and Pattern Recognition, Xi'an Jiaotong University, Xi'an,
Shaanxi 710049, China

Purpose: Presence of metal artifacts is a major reason of degradation of computed tomography image quality and there is still no standard solution to this issue. A class of recently investigated metal artifact reduction (MAR) methods based on forward projection of a prior image that is artifact-free to replace the metal affected projection data have shown promising results. However, usually it is hard to get a good prior image which is close to the true image without artifacts. This work aims at creating a good prior image so that the forward projection can replace the metal affected projection data well.

Methods: The proposed method consists of four steps based on the forward projection MAR framework. First, metal implants in the reconstructed image are segmented and the corresponding metal traces in the projection domain are identified. Then the prior image is obtained by two steps. A processed precorrected image is generated as an initial prior image first and then in the next step it is used as the initial image of the iterative reconstruction from the unaffected projection data to generate a better prior image. In order to deal with severe artifacts, the iteration incorporates the total variation minimization constraint as well as a novel constraint which forces the soft tissue region near metal to be as flat as possible. Finally, the projection is completed using forward projection of the prior image and the corrected image is reconstructed by FBP. A linear interpolation MAR method and two recently reported forward projection based methods are performed simultaneously for comparison.

Results: The proposed method shows outstanding performance on both phantoms' and patients' datasets. This approach can reduce artifacts dramatically and restore tissue structures near metal to a large extent. Unlike competing MAR methods, it can effectively prevent introduction of new artifacts and false structures. Moreover, the proposed method has the lowest RMSE in regions of both soft tissue and bone tissue among the corrected images and is ranked as the best method for evaluation, by radiologists.

Conclusions: Both subjective and quantitative evaluations of the results demonstrate the superior performance of the proposed algorithm, compared to that of the competing methods. This method offers a remarkable improvement of the image quality. © *2013 American Association of Physicists in Medicine*. [http://dx.doi.org/10.1118/1.4794474]

I. INTRODUCTION

Clinically, metallic implants such as surgical clips, dental fillings, and hip prosthesis result in streak artifacts in reconstructed images of x-ray computed tomography (CT), which degrades image quality severely.[1] Metal artifacts can be attributed to many effects, such as beam hardening due to the polychromatic x-ray spectrum, scatter and very low signal-to-noise ratio from photon starvation.[2,3] Currently, metal artifacts remain a major problem in x-ray CT.

In the past three decades, various metal artifact reduction (MAR) algorithms have been proposed. Among them,

some algorithms model the physics of data acquisition, such as beam hardening and noise, and then reconstruct the image iteratively from all the projection data,[4–6] whereas most of MAR methods try to reconstruct images only using the unaffected projection data, while projection data affected by metal, which is called metal trace or metal shadow, are considered to be missing. A simple and direct way is to complete the missed projections by the interpolation,[7–15] using data surrounding the metal shadowed area, and linear interpolation (LI) (Refs. [7–9]) is a commonly used interpolation algorithm. Interpolation methods are computationally efficient, however, sometimes new artifacts are introduced in the corrected images.[16]

Recently, the forward projection based methods have provided ways to complete the projection data by forward projecting a prior image,[17–21] which is built to be sufficiently similar to the distribution of the true image (the metal-free image) and is artifact-free. In arithmetic, the forward projection based methods usually share the workflow as follows. A precorrected image is reconstructed first by applying interpolation for metal traces completion, then based on a tissue-class model,[18,19] the reconstructed image is segmented into different material tissues and each tissue is assigned a uniform value, thereby obtaining the named prior image. The final projection for metal traces is acquired by forward projection of the prior image which is the same as real CT scanning. Bal and Spies[19] employed the k-means cluster technique to segment the adaptively filtered image into five classes, while Prell *et al.*[18] and Meyer *et al.*[21] segmented the precorrected image (or the uncorrected image with minor artifacts[21]) into air, soft-tissue, and bone equivalent materials by using two thresholds to obtain a prior image. Comparatively, dividing image into five tissues may lead to wrong segmentation,[18] which can be avoided by the three-tissue-class model to some extent. Despite that, wrong segmentation remains a problem in the presence of severe metal artifacts such as dental fillings, which may results in some false structures.[22] This is discussed further in this paper.

As the metal artifact reduction problem can be treated as the exterior problem, one possible way is to reconstruct the image from the unaffected projections iteratively, with adequate regularization. In this case, the image can be reconstructed by the expectation maximization (EM) method, the algebraic reconstruction technique (ART) and the maximum-likelihood algorithm for transmission tomography (MLTR).[23–26] Moreover, the penalized weighted least-squares (PWLS) constrained optimization method[27] is also applied to remove metal artifacts. Especially, the recently proposed compressed sensing (CS) theory is powerful to be used to recover signals from fewer measurements than are required by Nyquist–Shannon sampling theorem. As a result, the total variation (TV) minimization constrained method is widely used to reconstruct CT images from various cases of incomplete projections, such as few-views, limited angle data, and interior tomography.[28–31] Meanwhile, the TV constrained algorithmic framework has also been adopted to remove metal artifacts.[31–34] In general, iteration methods can reduce metal artifacts dramatically but the correction performance is dependent upon selection of regularization parameters to some extent. In addition, these methods are computationally time consuming which hinders their application in commercial CT.

To balance the image quality and computational efficiency, hybrid techniques can compensate for a single method's shortcomings.[35] Xia *et al.*[36] adopted B-spline interpolation followed by EM reconstruction to obtain a precise reconstruction of metal with low computational cost. A similar method was proposed by Choi *et al.*[37] who adopted CS theory. Boas and Fleischmann[38] proposed a metal deletion technique (MDT) with four iterations. In each iteration, an edge-preserving blur filtering, forward projection, and FBP reconstruction are performed. Lemmens *et al.*[20] proposed a MAR algorithm that consists of three iterative reconstructions and one projection completion procedure. The reconstructions include MLTR reconstructions and a maximum *a posteriori* (MAP) reconstruction incorporating constraints of multimodal priors. MDT and Lemmens' method can suppress metal artifacts remarkably.

Based on the forward projection MAR framework, we focus on finding a good prior image in an iterative way, with low computational time consumption. To this end, a TV constrained reconstruction is adopted to generate a prior image that is close to the ground truth. Furthermore, to deal with the severe ill-posed problem in the vicinity of metals, the TV constrained reconstruction is combined with a specifically designed uniformity constraint in the vicinity of metals. Initialized by a processed streak-free image, reconstruction needs only two main loop iterations to achieve a good prior image. Thereafter, the forward projection is performed and projections are then completed. The proposed method is evaluated on both simulated datasets and clinical datasets.

II. METHODS

The MAR methods, which complete sinogram by using forward projection of a prior image, can achieve good results as long as the prior image is close enough to the ground truth. Nevertheless, most of these MAR methods generate the prior image in a simple way, and the prior image is usually not perfect enough if the precorrected image still contains severe artifacts. In this work, we adopt the TV constraint based iterative reconstruction with an extra local constraint to get a good prior image, which we call the constrained prior image. Besides, in order to accelerate convergence, the iteration starts from an initial prior image which is a processed precorrected image with only a few artifacts. How to get a good prior image is the core in this work and is described in detail in the following.

The proposed MAR method follows a framework similar to other MAR methods based on forward projection, while the prior image is obtained in an iterative way. Hence, the proposed method can be referred to as a hybrid metal artifact reduction (HMAR) method. The proposed HMAR method consists of four main steps: (1) metal trace segmentation; (2) initial prior image generation; (3) constrained prior image generation; and (4) projection completion followed by the
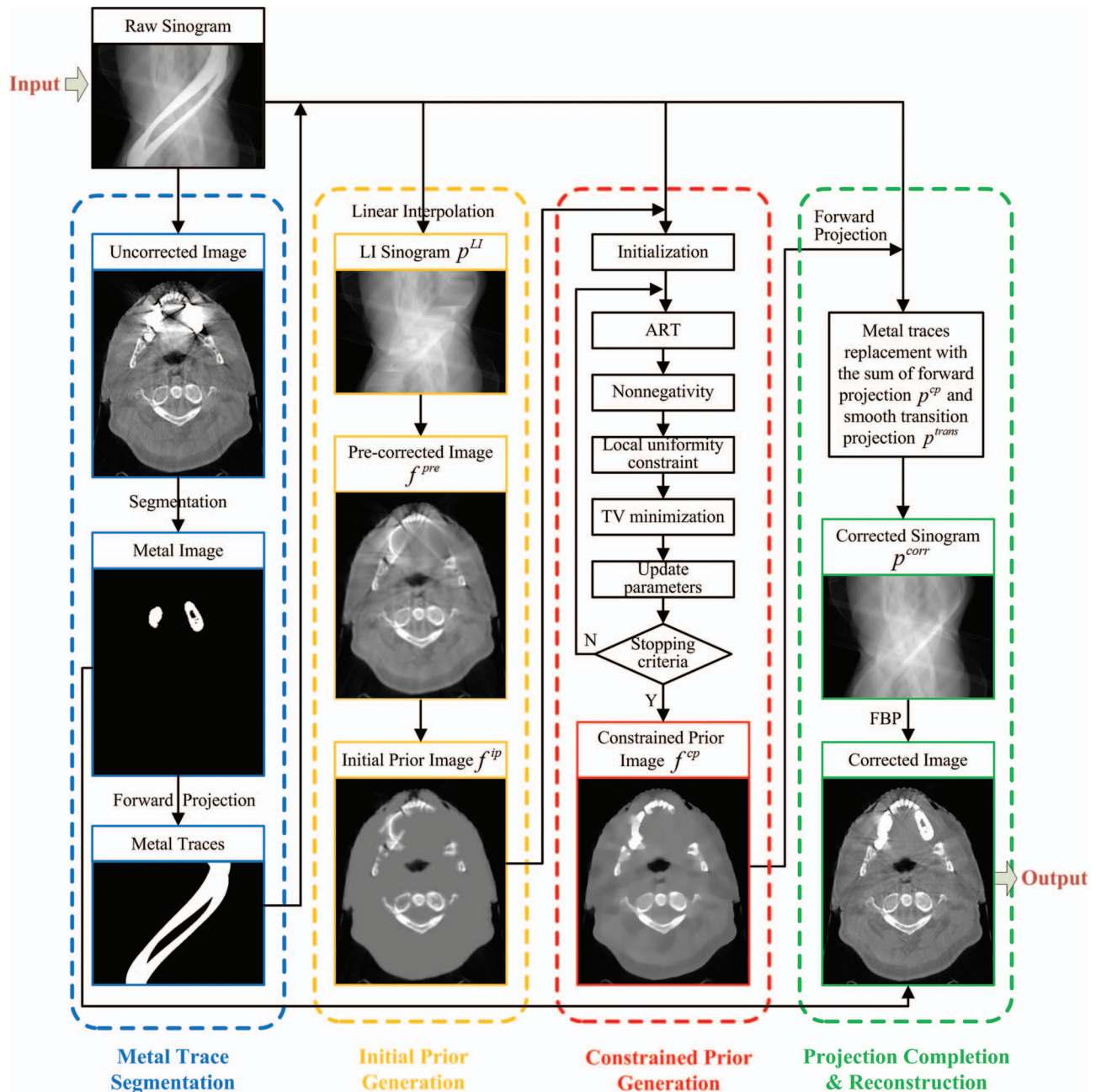
FIG. 1. Illustration of HMAR method. Note that p^{LI}, p^{cp}, p^{trans}, p^{corr}, f^{pre}, f^{ip}, and f^{cp} are all 1D vectors, for better vision, they are reformatted to the corresponding 2D image in this figure.

FBP reconstruction. The scheme of HMAR method is as depicted in Fig. 1. In these four steps, Steps 1 and 4 are very similar to the forward projection-based MAR algorithm (abbreviated to FP-MAR),[24] while Step 3 is the core of the proposed HMAR algorithm and Step 2 chooses a good initialization for iteration of Step 3 to accelerate convergence.

II.A. Metal trace segmentation

In this part, the metal trace in the original raw sinogram is extracted. This work is similar to Refs. 38 and 39. At first, the distorted image is reconstructed directly from the original

sinogram by FBP. Second, the metal image is segmented from the reconstructed image by the simple thresholding method. In this work, 3000 HU is selected as the threshold, which is proper to extract metal according to the literature.[38,39] In the uncorrected image, pixel value remains if it is greater than the threshold; else it is set to zero. Thus, the metal image is obtained. Finally, the forward projection is performed on the metal image to generate the metal projection. In the metal projection, the pixels with the value greater than zero are regarded as in the metal trace, i.e., the pixels are contaminated by the metal. These pixels in the raw sinogram are replaced in the fourth step.

II.B. Initial prior image generation

This step is similar to the tissue-class model[18,19,40] with some improvements. First, the raw sinogram is processed by the LI to replace the affected projections. In this paper, projection datasets and images are expressed by column vectors, and a vector variable with a subscript denotes the element of the vector. For example, given the raw projection dataset p with V views by B detector bins, one of its elements, the vth view bth bin pixel in the 2D projection dataset is denoted as p_j, $j = (v - 1) \times V + b$. In each view of the raw projection, if $\{p_k | k \in [j+1, j+\Delta].\}$ is metal trace and its neighboring projection pixels p_j, $p_{j+\Delta+1}$ are unaffected by metal, the LI processed projection data are obtained, as follows:

$$p_k^{LI} = p_j + \frac{p_{j+\Delta+1} - p_j}{\Delta + 1}(k - j).\qquad(1)$$

To suppress the influence of noise, p_j, $p_{j+\Delta+1}$ can be smoothed in advance with its neighboring pixels along both views and bins direction, but excluding pixels in the metal traces. The precorrected image is reconstructed from the LI processed sinogram p^{LI} and is then followed by Gaussian filtering, denoted by $f^{\text{pre}} = \{f_i^{\text{pre}}, i = 1, \cdots, N\}$, where N is the number of image pixels. The initial prior image f^{ip} is

then obtained from the precorrected image f^{pre} by the following process. For one thing, soft tissue equivalent materials account for a dominating proportion in most reconstructed CT images of humans and the soft tissue equivalent materials are easily distorted by metal artifacts; for another, compared with bone tissues, soft tissues have relatively low variance. Therefore, for the MAR method presented in Ref. 40, all pixel intensities between -500 and 500 HU are replaced with the mean value of these pixels to generate the prior image by which the streak artifacts are removed. Inspired by Ref. 40, we also remove the artifacts contained in the soft tissue equivalent materials in the same way. However, both Ref. 40 and tissue-class model[18,19] assign a uniform value to the segmented tissue or air, which may cause artificial jump edge between different classes of tissues and, even worse, false structures in the prior image.[22] To avoid this drawback, a smooth transition between the soft tissue and the others is necessary. Therefore, we introduce a weight coefficient vector ω according to the spatial distance between a soft tissue pixel and its nearest nonsoft-tissue (bone and air) pixel. The soft tissue pixels are assigned the weighted combination of the precorrected pixels' value and their mean value. So the ith pixel f_i^{ip} in the initial prior image f^{ip} is assigned the value defined by the formula (2),

$$f_i^{\text{ip}} = \begin{cases} (1-\omega_i) \cdot f_i^{\text{pre}} + \omega_i \cdot \text{mean}_{\text{soft}}, & -500 \text{ HU} \le f_i^{\text{pre}} \le 500 \text{ HU} \\ f_i^{\text{pre}}, & \text{others} \end{cases},\qquad(2)$$

where $\text{mean}_{\text{soft}}$ denotes the mean value of the segmented soft tissues and weight vector ω is defined as

$$\omega_i = \begin{cases} \frac{d_i}{D}, & d_i < D \\ 1, & d_i \ge D \end{cases}, \quad \forall i,\qquad(3)$$

where d_i indicates the Euclidean distance between the ith soft tissue pixel and its nearest nonsoft-tissue pixel in 2D image and parameter D controls the region size of smooth transition and is empirically set to 6 in this investigation.

II.C. Constrained prior image generation

In this section, we produce the prior image by using constrained iterative reconstruction. TV minimization constrained reconstruction can recover some information lost because of metals shadowing from the unaffected projection dataset. The CT image f can be reconstructed by solving the following constrained minimization:

$$f = \arg\min_f \|Mf - p^{\text{nonmetal}}\|_2^2$$
$$+ \lambda_1 \|f\|_{\text{TV}}, \ s.t. \ f_i \ge 0, \forall i,\qquad(4)$$

where the system matrix M consists of $(V \times B)$ row vectors M_i used to yield each projection of ray path, subject to $p_i^{\text{nonmetal}} = M_i f$. p^{nonmetal} is the unaffected projection dataset vector, λ_1 is the regularization parameter. $\|\cdot\|_2$ denotes two-norm. In objective function (4), the first term is data fidelity and $\|f\|_{\text{TV}}$ is TV regularization, calculated as $\sum_{x,y} \sqrt{(f_{x,y} - f_{x-1,y})^2 + (f_{x,y} - f_{x,y-1})^2}$, where (x, y) represents the pixel index of the 2D image.

As the metal is assumed to be opaque, x-rays passing through the metal are unavailable and image pixels near the metal miss more projection information required for their reconstruction. Even worse, the projection data are lost almost completely for pixels next to a large metal. As a result, for image pixels around large metals, the reconstructed value is not so reliable. So we propose to raise stronger regularization near the metal area to suppress unforeseen artifacts that may exist. To this point, we develop the new constraint acting on the soft tissue region near the metal, referred to as the local uniformity constraint (LUC). As is known, attenuation coefficients of soft tissue do not vary significantly in CT images, so the proposed LUC is to constrain the local region around metal to be as flat as possible. Namely, these soft tissue pixels near a metal should be close to a uniform value. Combined with the LUC, the new objective function can yield a better prior image that is referred to as the constrained prior image

f^{cp}. Thus the objective function of TV reconstruction with LUC (denoted as the TV-LUC) is stated as follows:

$$\boldsymbol{f}^{cp} = \arg\min_f \|\boldsymbol{M}\boldsymbol{f} - \boldsymbol{p}^{\mathrm{nonmetal}}\|_2^2 + \lambda_1 \|\boldsymbol{f}\|_{\mathrm{TV}}$$

$$+ \lambda_2 U(\boldsymbol{f}), \ s.t. \ f_i \geq 0, \forall i, \tag{5}$$

where $U(\boldsymbol{f})$ is the LUC term and λ_2 is the corresponding regularization parameter. $U(\boldsymbol{f})$ is defined as

$$U(\boldsymbol{f}) = \frac{1}{2} \sum_{i=1}^{N} (\upsilon_i \cdot (f_i - C_i))^2, \tag{6}$$

where $\boldsymbol{\upsilon}$ is a LUC weight vector with the range [0, 1] for each element and $\boldsymbol{C}$ is named the LUC uniform vector of a piecewise constant vector, in which soft tissue pixels in the vicinity of a metal are assigned a uniform value. Here, $U(\boldsymbol{f})$ is to constrain the image $\boldsymbol{f}$ as close to vector $\boldsymbol{C}$ as possible and

vector $\boldsymbol{\upsilon}$ controls the intensity of the constraint at each pixel. In the following, we draw the details of computation of the two vectors $\boldsymbol{\upsilon}$ and $\boldsymbol{C}$.

The LUC weight vector $\boldsymbol{\upsilon}$ is constructed in the following way. First, the local region around a metal can be defined by a parameter Dm. Soft tissue pixels with distances from the metal smaller than Dm compose the local region around this metal. Thus, the corresponding constraint weight is set to zero for any pixel beyond local regions. Second, let dm_i be the Euclidean distance between the ith image pixel f_i and its nearest metal pixel, then the corresponding constraint weight υ_i increases monotonously with the decrease of distance dm_i. In addition, the previously mentioned weight vector $\boldsymbol{\omega}$ is also considered in the transition region between the soft tissue and the others. To sum up, $\boldsymbol{\upsilon}$ can be constructed as Eq. (7),

$$\upsilon_i = \begin{cases} \omega_i \cdot \max\left\{1 - \frac{dm_i}{Dm}, 0\right\}, & \text{if the ith pixel is soft tissue} \\ 0, & \text{others} \end{cases}, \quad i = 1, \ldots, N. \tag{7}$$

As to the LUC uniform vector $\boldsymbol{C}$, a simple way is to assign each element of $\boldsymbol{C}$ a weighted mean value of the local regions, i.e., $\langle \boldsymbol{f}, \boldsymbol{\upsilon} \rangle / \|\boldsymbol{\upsilon}\|_2$, where $\langle \cdot, \cdot \rangle$ denotes the inner product. However, attenuation coefficients of different kinds of soft-tissue equivalent tissues (e.g., fat and muscle) may differ a little from each other, hence we compute $\boldsymbol{C}$ for each local region independently. For this purpose, label vector $\boldsymbol{L}$ with the same size as $\boldsymbol{\upsilon}$ is introduced to label the group of pixels that shares the same uniform value. In $\boldsymbol{L}$, the local region for each metal is assigned a unique nonzero label and the rest of the pixels are set to zero. Additionally, if two or more local regions are connected, their labels are an identical value. In this way, vector $\boldsymbol{L}$ is obtained and local region pixels are clustered into several groups. Then the LUC uniform value of $\boldsymbol{C}$ for each group of pixels is calculated by the mean of $\boldsymbol{f}$ weighted by $\boldsymbol{\upsilon}$ and masked by $\boldsymbol{L}$. The constraint on the remaining pixels whose LUC weights are zero is invalid and thus the corresponding C_i are simply set to zero. Then, each pixel value of the LUC uniform vector $\boldsymbol{C}$ can be obtained as stated in formula (8), where $\delta(\cdot)$ is Kronecker delta function, i.e., $\delta(t) = 1$ if $t = 0$, and $\delta(t) = 0$ if $t \neq 0$. An example of LUC weight vector $\boldsymbol{\upsilon}$ and LUC uniform vector $\boldsymbol{C}$ of a numerical jaw phantom is shown in Fig. 3,

$$C_i = \begin{cases} \dfrac{\sum\limits_{k=1}^{N} \upsilon_k f_k \delta(L_k - L_i)}{\sum\limits_{k=1}^{N} \upsilon_k \delta(L_k - L_i)}, & \text{if } \upsilon_i > 0 \\ 0, & \text{if } \upsilon_i = 0 \end{cases}, \quad i = 1, \cdots, N. \tag{8}$$

Similar to other TV constrained reconstruction algorithms,[28–31] the minimization of the three terms of objective function (5) as well as the non-negativity constraint

are iteratively performed in an alternating manner. The workflow of TV-LUC algorithm is presented as below. The symbol : = means assignment. The algebraic reconstruction technique (ART) (Ref. 41) is adopted to minimize the projection data fidelity term. In order to accelerate the algorithm, we make use of the ordered subset (OS) technique[42] in the ART procedure. In this paper, all numerical and clinical projection datasets are identically grouped into 10 subsets and thus the algorithm consists of 20 subiterations (2 main loops × 10 subsets). In each subiteration, ART operates on projections of only one subset. Moreover, to further accelerate the convergence, the iterative reconstruction starts with the initial prior image f^{ip}. Followed with each OS-ART subiteration, non-negativity, LUC and TV minimization are performed in sequence, where LUC and TV minimization are accomplished by using the gradient descent method and $[\cdots, \frac{\partial U(f)}{\partial f_i}, \cdots]^T$ and $[\cdots, \frac{\partial \|f\|_{\mathrm{TV}}}{\partial f_i}, \cdots]^T$ are gradient vectors of LUC and TV, respectively. To avoid the singularity when computing $\partial \|f\|_{\mathrm{TV}} / \partial f_i$, a small positive number is introduced to obtain approximate derivatives.[28] We minimize the TV term with implementation similar to the one described in Ref. 28. The factor da in Eq. 11 is defined by the difference between $\boldsymbol{f}$ of the previous and the current subiterations, which can be used as a parameter to control the strength of TV. At the end of each subiteration, the corresponding parameters, such as β, λ_2, and Dm, and vectors $\boldsymbol{\upsilon}$ and $\boldsymbol{C}$, are updated. Gradual decreasing of the parameters helps convergence of the algorithm. The image $\boldsymbol{f}^{\mathrm{cp}}$ is obtained after two main loop iterations. Finally, each metal pixel's value of $\boldsymbol{f}^{\mathrm{cp}}$ is replaced with its nearest nonmetal pixel's value, as in Ref. 18. Then, this $\boldsymbol{f}^{\mathrm{cp}}$ is the final prior image of the proposed HMAR method. In the workflow of TV-LUC

TV-LUC algorithm:

Initialization:

    Parameters: main loop iteration number $N_{main} := 2$, the number of subsets $Nos := 10$, $\beta := 1$, $\beta_{red} := 0.95$, $\lambda_1 := 0.2$, $\lambda_2 := 1$, $\lambda_{red2} := 0.98$, $Dm := 40$, $Dm_{red} := 0.98$.

    Initial image $\boldsymbol{f} := \boldsymbol{f}^{ip}$, $\boldsymbol{f^0} := \boldsymbol{f}$, LUC weight vector $\boldsymbol{v}$, LUC uniform vector $\boldsymbol{C}$.

Main loop:

for $n = 1$: N_{main} do:

  for $nos = 1$: Nos do:

    (A) OS-ART : for $i \in \{index\ of\ the\ nos^{th}\ subset\ projections\}$ do:

$$\boldsymbol{f} := \boldsymbol{f} + \beta \boldsymbol{M}_i \frac{\boldsymbol{p}^{nonmetal} - \boldsymbol{M}_i \cdot \boldsymbol{f}}{\boldsymbol{M}_i \cdot \boldsymbol{M}_i}; \qquad (9)$$

    (B) Nonnegativity: for $i = 1$: N do:

      if $f_i < 0$ then $f_i := 0$;

    (C) Local uniformity constraint: for $i = 1$: N do:

$$f_i := f_i - \lambda_2 \cdot \frac{\partial U(\boldsymbol{f})}{\partial f_i} = f_i + \lambda_2 \cdot v_i \cdot (C_i - f_i); \qquad (10)$$

    (D) TV minimization:

$$da := \left\| \boldsymbol{f^0} - \boldsymbol{f} \right\|_2, \boldsymbol{f^0} := \boldsymbol{f};$$

      for $k = 1$: 20 do:

        Gradient vector of TV norm: $\boldsymbol{d}f := \nabla_f \|\boldsymbol{f}\|_{TV} = \left[\cdots, \frac{\partial \|\boldsymbol{f}\|_{TV}}{\partial f_i}, \cdots \right]^T$,

        Normalization: $\boldsymbol{d}f := \boldsymbol{d}f / \|\boldsymbol{d}f\|_2$,

$$\boldsymbol{f} := \boldsymbol{f} - \lambda_1 \cdot da \cdot \boldsymbol{d}f; \qquad (11)$$

      end

    (E) Update data: $\beta := \beta \cdot \beta_{red}$, $\lambda_2 := \lambda_2 \cdot \lambda_{red2}$, $Dm := Dm \cdot Dm_{red}$, update $\boldsymbol{v}$ and $\boldsymbol{C}$.

  end

end

Output: $\boldsymbol{f}^{cp} := \boldsymbol{f}$

---

reconstruction algorithm, empirically selected parameters are fixed for all phantom and clinical datasets in this study.

Objective function (5) consists of three terms: the data fidelity term, TV constraint term and LUC term. Obviously, the former two terms are convex. As to the LUC term, vectors $\boldsymbol{v}$ and $\boldsymbol{C}$ are determined by the previous subiteration and thus they can be treated as constant vectors in the current subiteration. Therefore, the LUC term is convex in each subiteration since it is a quadratic function with respect to $\boldsymbol{f}$. However, we cannot prove convexity of the cost function since the dependence of LUC vectors on iteration of $\boldsymbol{f}$ makes the cost function complicated. But the experimental results in Sec. IV show that the constrained optimization can work well and good prior images can be obtained in this study.

II.D. Projection completion and image reconstruction

In this step, forward projection $\boldsymbol{p}^{cp}$ of the constrained prior image $\boldsymbol{f}^{cp}$ is obtained by the ray-driven method[52] to complete the sinogram and the corrected image is finally reconstructed from the corrected sinogram. However, if the metal trace pixels are replaced with the corresponding ones of $\boldsymbol{p}^{cp}$ directly, it leads to discontinuity at the boundary of the metal traces. The discontinuity results in new streak artifacts. Therefore, elimination of the discontinuity is a necessary step to achieve a relatively perfect CT image. In this work, the LI method[7,39] is adopted again to generate a projection vector $\boldsymbol{p}^{trans}$ which is treated as a smooth transition between $\boldsymbol{p}^{cp}$ and the raw pro-

jection dataset $\boldsymbol{p}$. For each view, we have

$$
\begin{aligned}
p_k^{trans} = \left(p_j - p_j^{cp} \right) \\
+ \frac{\left(p_{j+\Delta+1} - p_{j+\Delta+1}^{cp} \right) - \left(p_j - p_j^{cp} \right)}{\Delta + 1} (k - j),
\end{aligned}
$$

(12)

where subscripts have the same meaning as in formula (1). Then corrected projection $\boldsymbol{p}^{corr}$ in the metal traces is stated as

$$p_k^{corr} = p_k^{cp} + p_k^{trans}. \qquad (13)$$

The remaining unaffected projections in $\boldsymbol{p}^{corr}$ have the same value as in the raw projection dataset. It can be seen from formulas (12) and (13) that the replaced projection data in metal traces can seamlessly connect to the surrounding unaffected projection data. Finally, the corrected image is reconstructed by using conventional FBP algorithm and segmented metals in the first step are inserted back into the corrected image.

III. EXPERIMENTAL MATERIALS

In this study, we first adopt simulation experiments to quantitatively compare the performance of the HMAR with competing methods. And then, the proposed and the competing methods are compared on the scanned datasets of patients and evaluated by two radiologists.
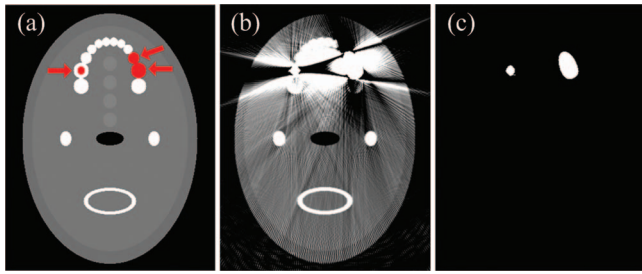
FIG. 2. Simulation of a numerical jaw phantom. (a) definition of the numerical jaw phantom, three metals are inserted into teeth as indicated by arrows. (b) reconstructed image of the phantom with metals, and (c) the segmented metals from (b). It can be seen in (c) that the two adjacent metals are combined into a large one.

FIG. 3. The LUC weight vector υ and the LUC uniform vector C of the numerical jaw phantom with metals. (a) the initial image of TV-LUC algorithm, and (b) and (c) the corresponding LUC weight vector and LUC uniform vector, respectively. (c) is piecewise constant, which consists of two uniform regions, C^0 and C^1.

In the simulation, a 2D numerical jaw phantom designed by Lemmens *et al.*[20] is adopted. The phantom consists of 512×512 pixels and 0.5×0.5 mm per-pixel, as shown in Fig. 2. Composition of soft tissues and bone tissues in the phantom is set according to the ICRU 44 Report and the x-ray attenuation coefficients of these tissues are obtained from XCOM.[43,44] Three amalgam dental fillings are inserted into the phantom as shown in Fig. 2(a). Projection datasets of the phantom with and without metals are simulated. The polychromatic x-ray is simulated and each detector bin receives 1 000 000 photons on average in the case of vacant scan; beam hardening effect and poisson noise are simulated.[45] The distance between the x-ray source and the rotation center is 100 cm and the distance between the x-ray source and detector is 150 cm. The projection is generated according to the equispatial fanbeam CT geometry with 512 detector bins and 660 projection views over $360°$.

The CatPhan® 600 phantom (The Phantom Laboratory, Inc., Salem, NY), the head-and-neck of two patients (patients 1 and 3) and the pel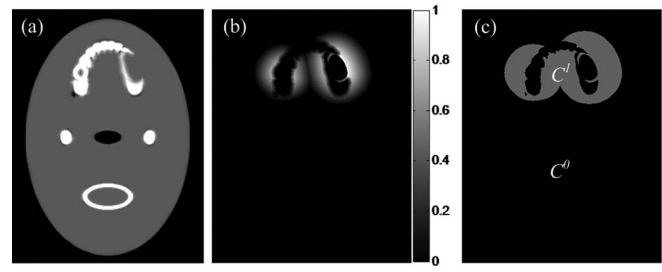vis of a patient (patient 4) were scanned on a kV onboard imaging (OBI) system integrated in a TrueBeam™ medical linear accelerator (Varian Medical System, Palo Alto, CA). The head of patient 2 was scanned on a Siemens SOMATOM Sensation 16 scanner CT using helical scanning geometry. After rebinning process, the acquired multislice dataset has been converted into a stack of fanbeam sinograms,[46] each associated with one horizontal z-slice. The measurements of CatPhan® 600 phantom, patients 1 and 3, were acquired with 364 projection views over $200°$ in full-fan mode with a bowtie filter and the measurement of patient 4 was acquired with 656 projection views over $360°$ in half-fan mode with a bowtie filter. For Varian Medical System, distances from the x-ray source to the rotation center and to the detector are 100 and 150 cm, respectively. Its imaging detector size is 30×40 cm consisting of 768×1024 pixels (0.388×0.388 mm per-pixel) and projection data at each view is down-sampled by a factor of 2. The measurement of patient 2 has 1160 projection views over $360°$ and the number of detector bins is 672, the corresponding FOV is 25 cm and distance from the x-ray source to the rotation center
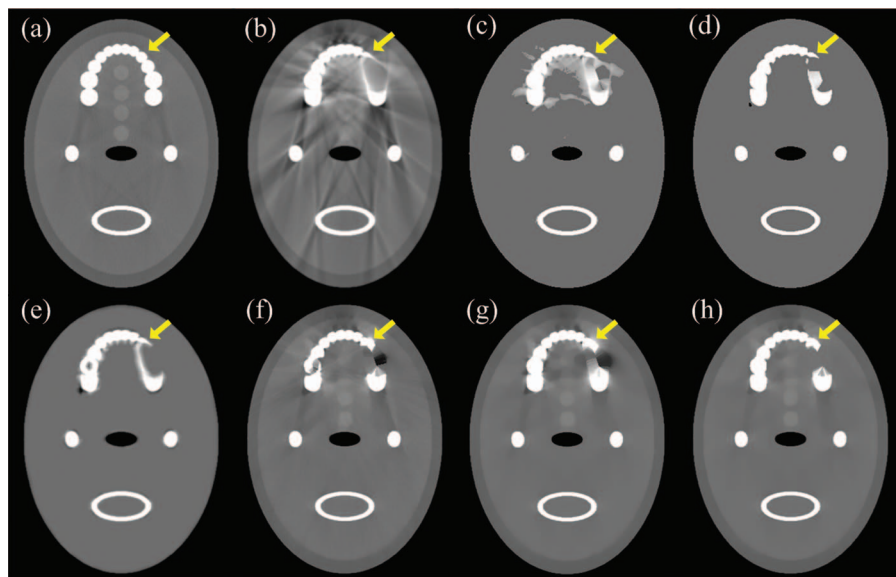

FIG. 4. Comparison of prior images. (a) reconstructed image of the jaw phantom without metals, which can be regarded as the ground truth. (b) the precorrected image by linear interpolation, and (c)–(h) the prior images for different methods. (c)–(e) are generated from (b), they are FP-MAR prior, NMAR prior and the proposed initial prior images, respectively. (f)–(h) are obtained by TV-LUC-zero, TV, and TV-LUC algorithms, respectively, in which (g) and (h) are initialized with (e). The image display window width and window level are (WW = 1500 HU, WL = 100 HU).
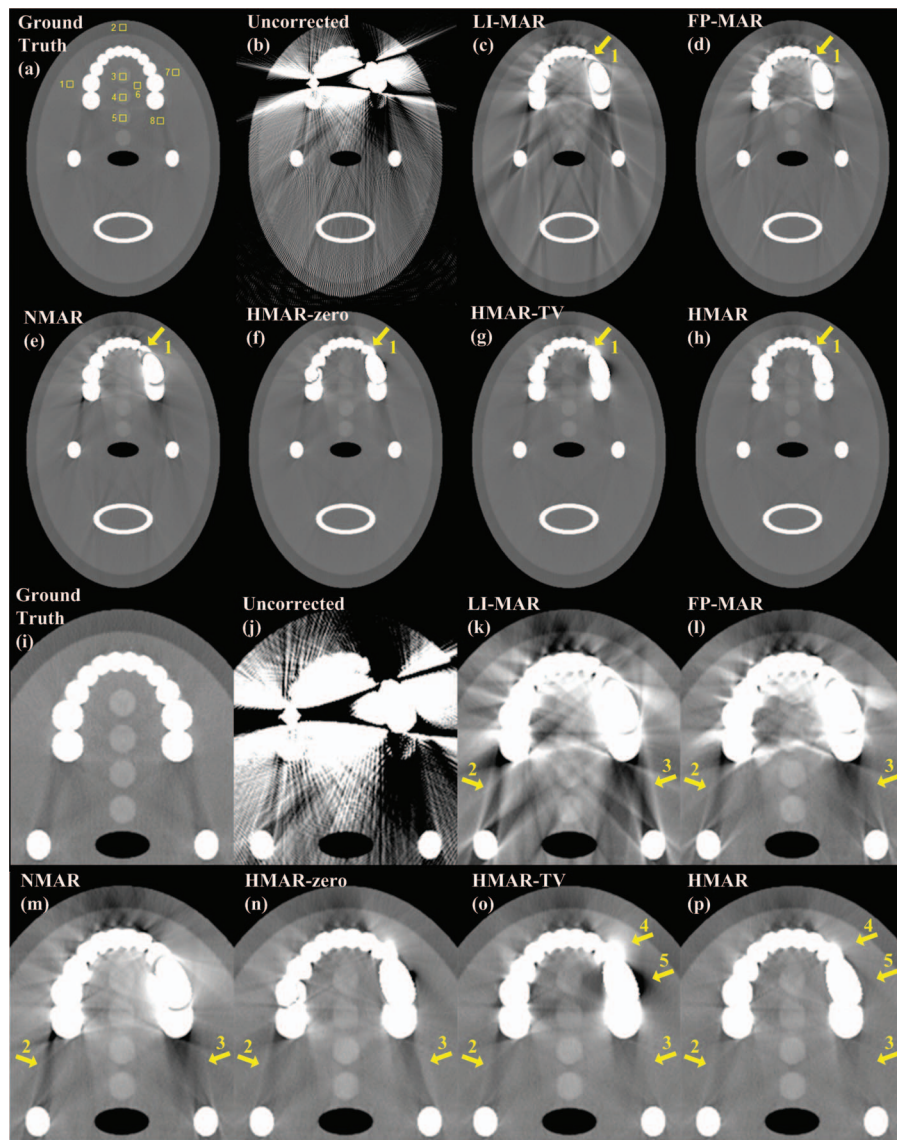
FIG. 5. The reconstruction of the numerical jaw phantom. (a) FBP reconstruction of the numerical jaw phantom without metallic implants, and (b) the uncorrected image with metallic implants. (c)–(h) the corrected results by LI-MAR, FP-MAR, NMAR, HMAR-zero, HMAR-TV, and HMAR, respectively. (i)–(p) correspond to the magnifications of partial (a)–(h), respectively. The window width and window level are (WW = 1500 HU, WL = 100 HU) for (a)–(h) and (WW = 750 HU, WL = 0 HU) for (i)–(p), respectively.

is 57 cm. The CT tube voltage is 100 kV for CatPhan® 600 phantom, patients 1 and 3, 120 kV for patient 2 and 125 kV for patient 4. The tube current is 140 mA for CatPhan® 600 phantom, 20 mA for patients 1 and 3 and 80 mA for patient 4; x-ray pulse length at each projection view is 13 ms for CatPhan® 600 phantom and 20 ms for patients 1, 3 and 4. Patient 2 was scanned with 496 mAs. The CatPhan® 600 phantom contains no metal in it, so we simulate three metals located in air holes of the phantom as illustrated in Fig. 8(b). The x-rays passing through the metals are regarded as metal traces, and the projection information is absolutely missing. There is almost no difference between this quasi-realistic case and the realistic case of metals inserted and we can hence assess the MAR methods objectively and quantitatively since the ground truth is known. Central slice projection data of CatPhan® 600 phantom is chosen for reconstruction. The chosen representative slices of patients 1, 3 and 4 are just a little far from the

central slice and, therefore, reconstruction and forward projection can be assumed approximately as 2D fanbeam case. The reconstructed slices of patients 1–4 contain dental fillings, a clip, a metal implant and a screw, respectively. All these reconstructed images are of 512 × 512 pixels, with pixel sizes 0.776 × 0.776 mm for CatPhan® 600 phantom, patients 1–3, and 1 × 1 mm for patient 4, which ensures that all scanned objects are contained in the reconstructed images. In addition, Parker weights[47] and offset detector weights[48, 49] are adopted to deal with short-scan (patients 1 and 3) and offset detector (patient 4) in reconstruction, respectively.

IV. RESULTS

In this paper, the linear interpolation MAR method, MAR method in Ref. 18, MAR method in Ref. 21, and the proposed method are denoted as LI-MAR, FP-MAR, NMAR,

and HMAR, respectively. FP-MAR is a typical forward projection based method for flat-detector CT, while NMAR can be regarded as an improved forward projection based method. The LI-MAR, FP-MAR, and NMAR methods are selected for comparison with the proposed HMAR. We implemented those methods because their codes are not available in public. We try to reproduce these methods faithfully except one detail for FP-MAR implementation. In its original literature, FP-MAR was proposed to deal with metal artifacts for flat-detector CT and the three-dimensional linear interpolation-based MAR was adopted to obtain a precorrected image. Since the proposed HMAR is to mainly deal with severe metal artifacts for 2D CT, for a fair comparison, the widely used LI-MAR (Refs. 7 and 39) is adopted to generate precorrected image in obtaining prior image for FP-MAR and NMAR.

In order to understand the TV-LUC reconstruction algorithm better, it is compared with its two degenerate versions, the iteration starting from uniform zero image rather than from f^{ip} (denoted as TV-LUC-zero algorithm) and the other is without LUC (denoted as TV algorithm). In implementation of the two versions, all parameters and procedures are the same as the TV-LUC algorithm. Correspondingly, the HMAR method is degenerated into two versions and denoted as HMAR-zero and HMAR-TV, which are implemented for comparison on phantom datasets. For convenient representation, HMAR-zero, HMAR-TV, and HMAR are collectively named as HMAR type methods.

Reconstructed images are displayed with different window settings. In each group of the illustrated images, arrows emphasize the positions of the metallic implants and the severe metal artifacts to be discussed. In order to evaluate the MAR methods quantitatively, several 8×8 ROIs are selected for analyzing their mean CT number and standard deviation (SD). The ROI position is chosen where the artifacts are severe. Moreover, in order to assess these methods globally, we compute the root mean square error (RMSE) between pixel intensities of the corrected images f^{corr} and the ground truth $f^{\mathrm{groundtruth}}$. Let the k-tissue be either soft tissue or bone tissue, then RMSE of the k-tissue is given by Eq. (14), where T_k indicates the set of the k-tissue pixels and N_k is the pixel number of the k-tissue,

$$\mathrm{RMSE}_{k-\mathrm{tissue}} = \sqrt{\frac{\sum_i \left(f_i^{\mathrm{corr}} - f_i^{\mathrm{groundtruth}}\right)^2}{N_k}}, \quad f_i^{\mathrm{corr}} \in T_k.$$

(14)

IV.A. Numerical jaw phantom

Figure 2 shows the simulated jaw phantom with dental fillings. The corresponding LUC weight vector and LUC uniform vector at the beginning of TV-LUC iteration are shown in Fig. 3. Figure 4 compares the prior images produced by various methods. Comparing images shown in Figs. 4(f)–4(h) with those in Figs. 4(c) and 4(d), the HMAR type methods can recover the variance in soft tissue and the tooth shape pointed by the arrow better. However, there exist obvious dark and bright artifacts in soft tissue region next to the large metal in Fig. 4(g), while the constrained prior image in Fig. 4(h) can prevent generation of such kind of artifacts by using LUC.

Figure 5 shows reconstructed images of the numerical jaw phantom before and after the corrections made by the
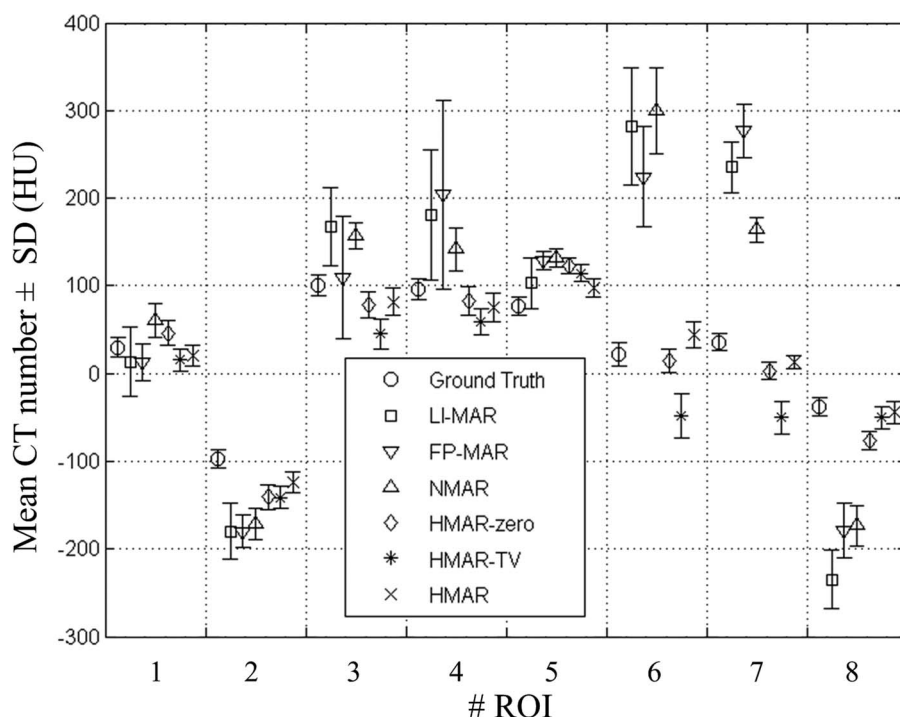

FIG. 6. Mean CT number and the SD for the ROIs in Fig. 5.

TABLE I. RMSE of soft tissue and bone in the numerical jaw phantom (HU).

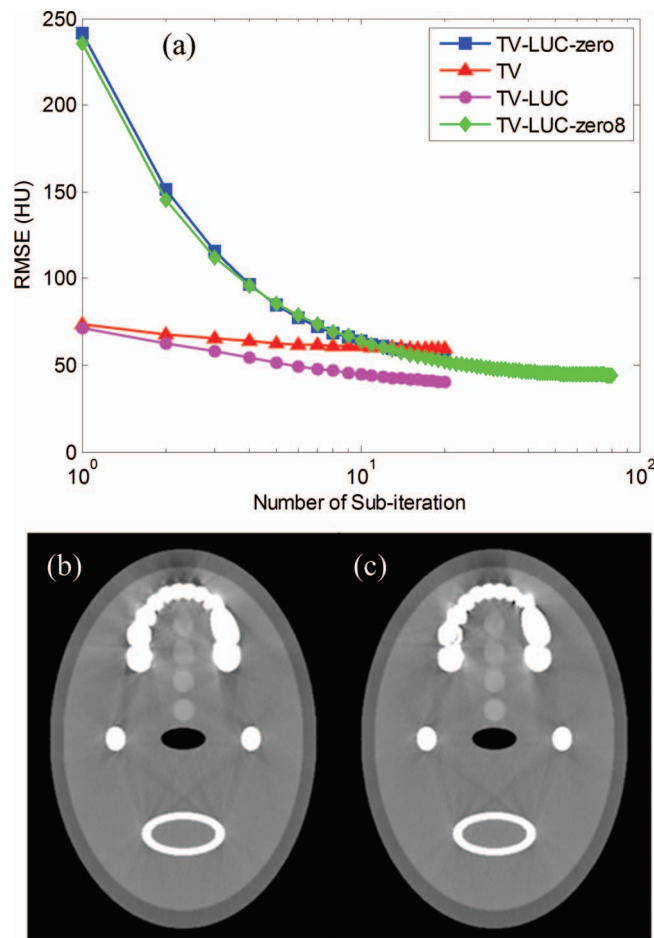|	LI-MAR	FP-MAR	NMAR	HMAR-zero	HMAR-TV	HMAR
Soft tissue	86.3	68.1	55.6	34.9	45.5	25.7
Bone	453.5	406.5	369.9	221.8	193.9	156.0

FIG. 7. (a) is RMSE of the four prior image generations versus the number of subiteration. The horizontal axis is the number of subiteration and the vertical axis is RMSE between the prior image at each subiteration and the ground truth (where the metal pixels are excluded). (b) is HMAR corrected image corresponding to Fig. 5(h). (c) is the corrected image by using the constrained prior image obtained by the TV-LUC-zero algorithm with 8 main loop iterations (TV-LUC-zero8) and with optimized parameters, in which the window width and window level are (WW = 750 HU, WL = 0 HU).

various MAR methods. Figure 5(a) is the reconstructed image without metallic implants, which can be regarded as the ground truth. As can be seen in Fig. 5(b), the uncorrected image suffers severe metal artifacts in the presence of multiple large dental fillings. All the six MAR methods can reduce metal artifacts in different degrees, among them HMAR corrected image is the closest to the ground truth, by observation. To be specific, the tooth pointed by arrow 1 is next to the large metal [refer to Fig. 4(a)] and its shape is distorted greatly in LI-MAR corrected image. For the results of FP-MAR and NMAR, as illustrated in Figs. 5(d) and 5(e), this bone tissue remains almost in the same distorted shape as in prior images shown in Figs. 4(c) and 4(d). While prior images of the HMAR-zero, HMAR-TV, and HMAR are all obtained by the constrained iterative reconstruction, the tooth can be restored to a large extent from information of the unaffected projection dataset. Hence, these three proposed methods can repair the tooth much better than the other three MAR methods, as can be seen in Figs. 5(c)–5(h). Regarding the streak artifacts

that remain after correction, we choose the regions pointed by arrows 2 and 3 for analysis. Clearly, the three HMAR type methods have better performance compared to the competing methods. Among them, result of the HMAR method has the lightest artifacts, while the performance of the LI-MAR is the worst. In addition, all the four small low contrast soft tissues located in the upper middle part of the phantom can be clearly observed in the NMAR and three HMAR type methods corrected images, among which the result of HMAR is the best. In comparison, only two or three low contrast tissues can be recognized after LI-MAR and FP-MAR corrections. From the crosswise comparative analysis among the three HMAR type methods, the HMAR corrected image is the best in Figs. 5(n)–5(p). It can be observed that the streak artifacts in Fig. 5(n) are relatively severe and there exist obvious bright and dark artifacts at the soft tissues pointed by arrows 4 and 5 in Fig. 5(o). In contrast, HMAR can reduce these artifacts and obtain pixel values very close to the ideal ones as shown in Fig. 5(p). To sum up, Figure 5 demonstrates that HMAR has better performance in artifacts suppression than the other MAR methods, especially for recognition of the low contrast structure and the bone tissue restoration near the large metal.

The mean CT number and the standard deviation of each ROI [refer to Fig. 5(a)] in each reconstructed image are shown in Fig. 6. Generally, HMAR has the mean CT number that is closest to the ground truth and also has the minimum standard deviation in most ROI. The maximum standard deviation of these 8 ROIs is about 13 HU in the ground truth image, and is about 16, 25, and 16 HU in the corrected images based on the HMAR-zero, HMAR-TV, and HMAR methods, respectively, while the data reach more than 50 HU in the other three corrected images. The biased errors of the mean CT number in ROI 6 and ROI 7 are smaller in HMAR corrected image, at around 21 and 23 HU, respectively, compared with more than 202 and 128 HU in LI-MAR, FP-MAR, and NMAR corrected images.

Table I shows that the three HMAR type methods can reach much lower RMSE for both soft tissue and bone than LI-MAR, FP-MAR, and NMAR. Specifically, the HMAR correction has the least RMSE for both soft and bone tissues. Comparison of data of the three HMAR type methods shows that the initialization with f^{ip} and the LUC in HMAR method have a positive effect on bringing down the RMSE.

Figure 7(a) shows the RMSE curves in the iteration process of TV-LUC-zero, TV, and TV-LUC with two main loop iterations as indicated before, as well as the TV-LUC-zero algorithm with eight main loop iterations (denoted as TV-LUC-zero8). It can be observed from Fig. 7(a) that RMSE of
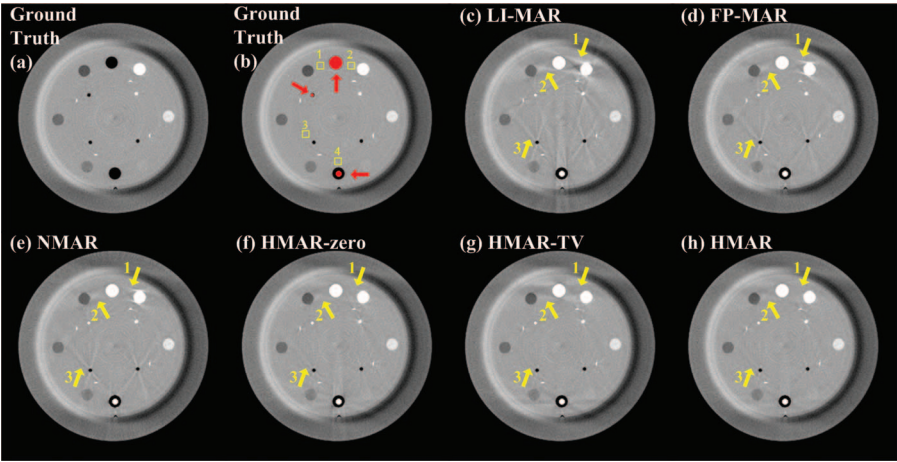
FIG. 8. The reconstruction of the CatPhan® 600 phantom. (a) FBP reconstructed image of the real scanned dataset without metal interts, and (b) simulates three metal inserts in the phantom as indicated with arrows. (c)–(h) the corrected results by LI-MAR, FP-MAR, NMAR, HMAR-zero, HMAR-TV, and HMAR, respectively. The window width and window level are (WW = 750 HU, WL = 0 HU).

TV-LUC decreases monotonically and TV-LUC can reach a RMSE lower than TV-LUC-zero and TV with two main loop iterations, so the LUC and initialization with f^{ip} are necessary to produce a good prior image with fewer iterations. Since we cannot prove the convexity of objective function (5), the algorithm might converge to different local minima with different initial values. But the simulation result shows that TV-LUC-zero8 can also reach a low RMSE which is very close to TV-LUC, and both the obtained prior image and the corrected image are much similar to the HMAR. It can be validated further by comparing the corrected images shown in Figs. 7(b) and 7(c). To sum up, a good initial initialization is helpful to fast achieve a good prior image in the iterations of TV-LUC.

IV.B. CatPhan® 600 phantom

Figure 8 shows experimental results on the real dataset scanned from the CatPhan® 600 phantom. Figure 8(a) is regarded as ground truth for the following evaluation. Three simulated metals pointed by arrows are inserted in the ground truth image, as shown in Fig. 8(b). It is clear that the artifacts are most severe in LI-MAR corrected image and are the lightest in images corrected by the three HMAR type methods, which is similar to the situation of the numerical phantom simulation. As indicated by arrow 1, the bright streak artifacts between the metal and the bone equivalent material are obvious in LI-MAR, FP-MAR, and NMAR corrected images, while the artifacts are removed completely in the three HMAR type methods corrected images. Similarly, the streak
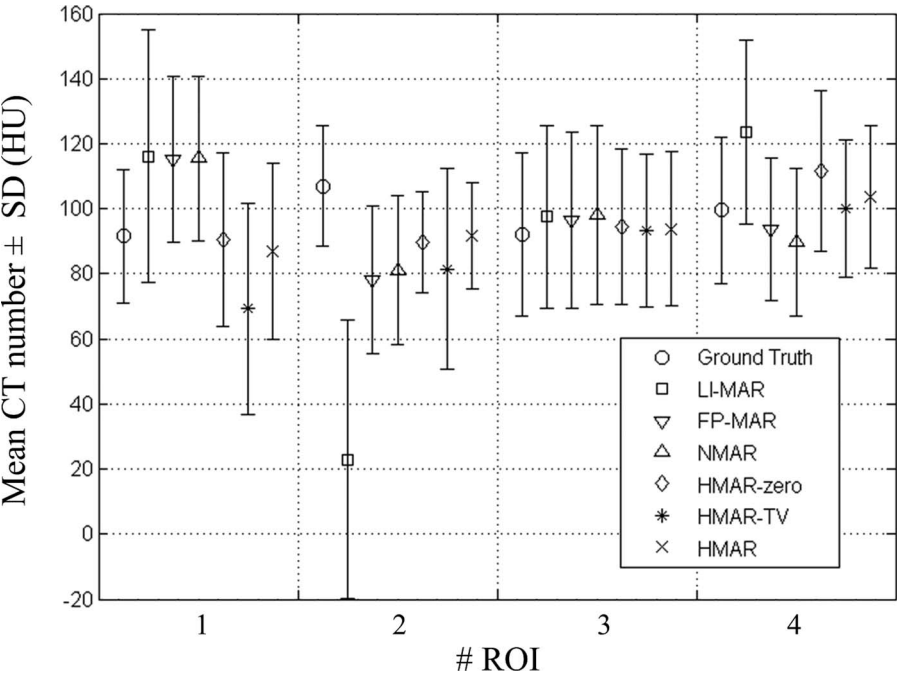

FIG. 9. Mean CT number and the SD for the ROIs in Fig. 8.

TABLE II. RMSE of soft tissue and bone equivalent materials in CatPhan® 600 phantom (HU).

	LI-MAR	FP-MAR	NMAR	HMAR-zero	HMAR-TV	HMAR
Soft tissue	18.4	13.4	13.1	11.6	13.0	11.0
Bone	105.7	39.5	35.5	14.3	18.0	14.2

artifacts indicated by arrows 2 and 3 in images corrected by the three HMAR type methods are weaker than that by LI-MAR, FP-MAR, and NMAR. Besides, the artifacts near the largest metal in HMAR corrected image are slightly weaker than in the HMAR-zero and HMAR-TV corrected images.

Figure 9 shows the mean CT number and the standard deviation of each ROI [refer to Fig. 8(b)] in the reconstructed images. Standard deviations of these 4 ROIs in FP-MAR, NMAR, and the three HMAR type methods corrected images are similar to the ground truth image. In general, the corrected images based on the three HMAR type methods have the mean CT number closer to the ground truth in these ROIs.

The RMSE of soft tissue and bone equivalent materials in CatPhan® 600 phantom is given in Table II. The data in Table II follow a trend similar to that in Table I. HMAR has the least RMSE for both the soft tissue and the bone equivalent materials, followed by HMAR-zero and HMAR-TV.

IV.C. Patients' measurements

Figure 10 shows head CT images of patient 1, in the presence of two big dental fillings distributed on both sides of the lower jaw. Since the metals are big and surrounded by both soft tissue and bone tissue, generally it is hard for MAR methods to get artifact-free results. It can be observed that there exist severe metal artifacts in the uncorrected images shown in Figs. 10(b) and 10(g). Although all these four MAR methods can reduce the artifacts significantly, as shown in Figs. 10(c)–10(f) and Figs. 10(h)–10(k), quality of images of the three competing methods is still unsatisfactory. They cannot remove the dark artifact in the soft tissue near the outer side of the teeth as indicated by the arrow 1. Even worse, some false structures emerge when the FP-MAR and NMAR methods are applied, as shown by arrows 2–4, which are easy to be taken for lesions or other tissue structures. HMAR can avoid introducing these new artifacts and reduce metal artifacts more effectively. Although some artifacts remain in the HMAR corrected image, they are lighter compared to images corrected by other MAR methods. The reason why HMAR can achieve such a good result is attributed to its better prior image.

In order to explain the mechanism of producing false structures in FP-MAR and NMAR corrected images and why HMAR is superior, we illustrate their prior images and two representative profiles in Fig. 11. All FP-MAR prior, NMAR prior, and initial HMAR prior classify some soft equivalent tissue wrongly as air, as pointed out by the arrow. The wrong classification tissue is repaired in the constrained HMAR
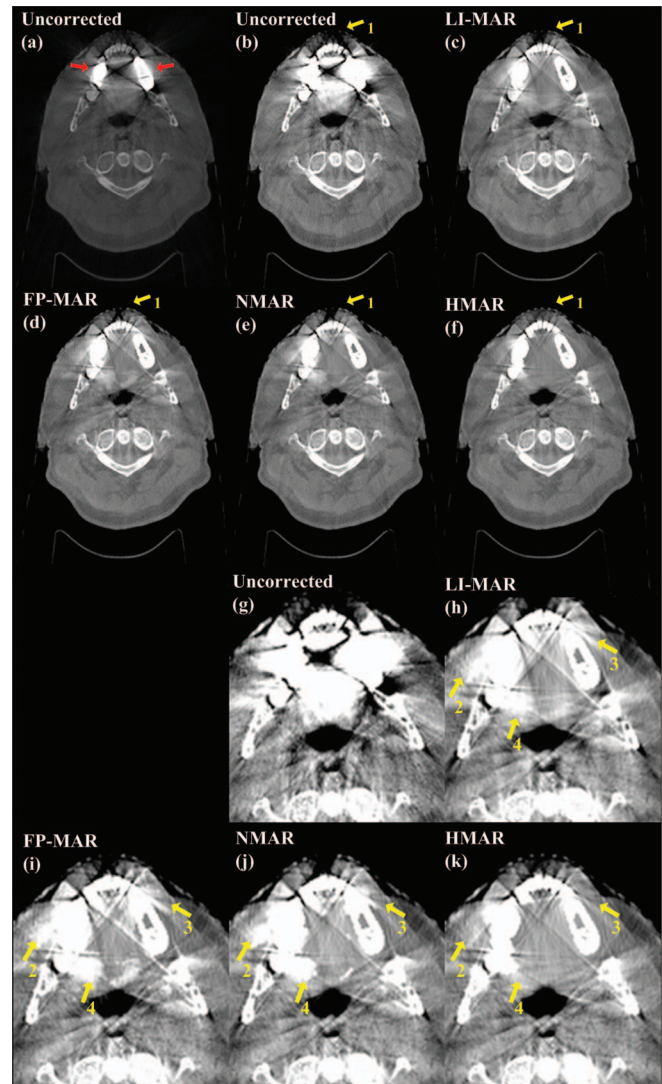

FIG. 10. Patient 1, slice through two big dental fillings distributed on both sides of the lower jaw. (a) and (b) the uncorrected images, the two arrows in (a) indicate the dental fillings. (c)–(f) the corrected results by LI-MAR, FP-MAR, NMAR, and HMAR, respectively. (g)–(k) correspond to the magnifications of partial (b)–(f), respectively. The window width and window level are (WW = 4000 HU, WL = 1000 HU) for (a), (WW = 1500 HU, WL = 100 HU) for (b)–(f), and (WW = 750 HU, WL = 0 HU) for (g)–(k), respectively.

prior image by its TV-LUC algorithm. Thus, only HMAR corrected image can restore the soft tissue. For clear illustration, two profiles in soft tissue region along with two lines, as indicated in Fig. 11(a), are shown in Figs. 11(f) and 11(g). Comparisons of the prior images are shown in Figs. 11(b)–11(e). All FP-MAR prior, NMAR prior, and initial HMAR prior images contain artifacts because the pixel intensities along the lines fluctuate around the soft-bone tissue threshold. Segmenting images by threshold causes discontinuity for FP-MAR prior and NMAR prior as shown in Figs. 11(f) and 11(g) (refer to the sharp fluctuation along the profiles). Thus, the false edges emerge and result in false structures in the corrected images. In contrast, the constrained HMAR prior adopts the iterative process to prevent the sharp false edges. As a result, artifacts in the initial prior image are suppressed
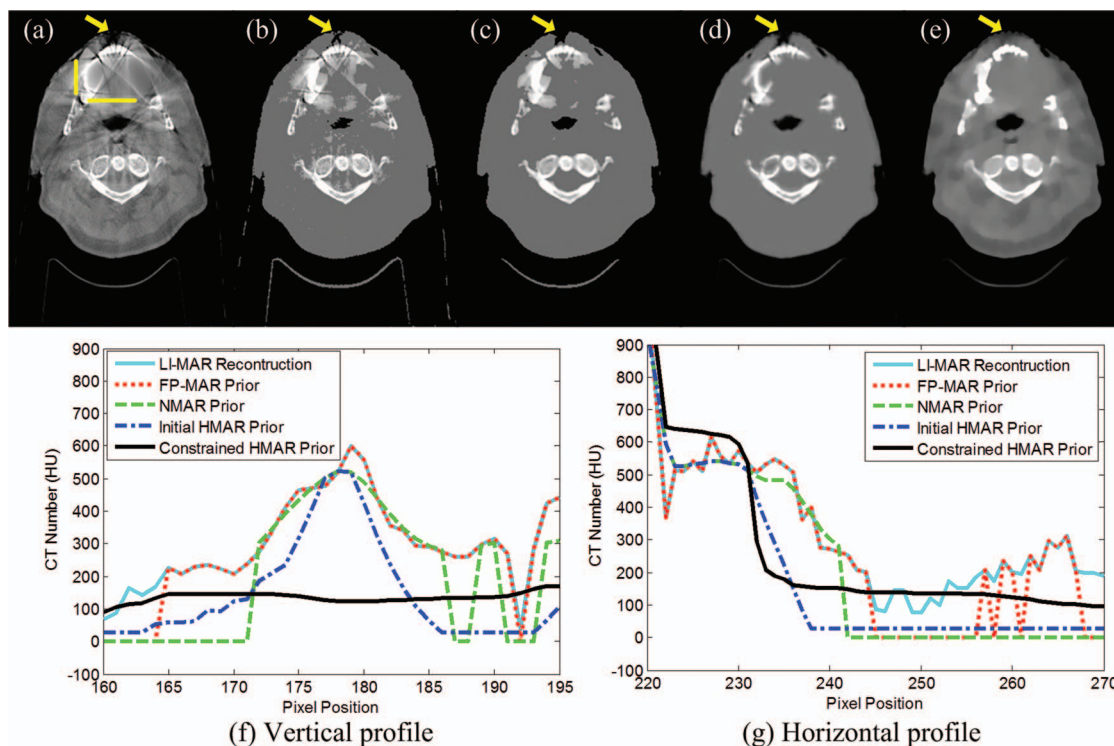
FIG. 11. Comparison of the prior images of MAR methods, (a) the LI-MAR reconstruction where the metals are not inserted back to the image, and (b)–(e) the FP-MAR prior image, NMAR prior image, initial HMAR prior image and constrained HMAR prior image, respectively, in which the window width and window level are (WW = 1500 HU, WL = 100 HU). (f) and (g) are the profiles comparison of the prior images at the vertical line and the horizontal line indicated in (a), respectively.
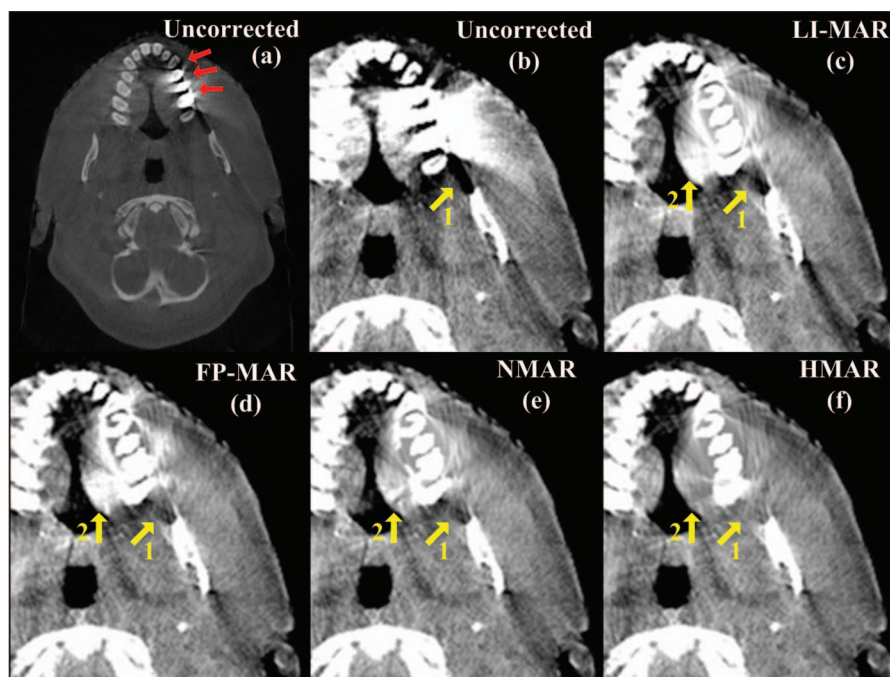

FIG. 12. Patient 1, slice through three adjacent dental fillings in the upper jaw. (a) and (b) the uncorrected images, the three arrows in (a) point out the dental fillings, and (c)–(f) the corrected results by LI-MAR, FP-MAR, NMAR, and HMAR, respectively. (b)–(f) are the magnifications of partial images. The window width and window level are (WW = 4000 HU, WL = 1000 HU) for (a) and (WW = 750 HU, WL = 0 HU) for (b)–(f), respectively.
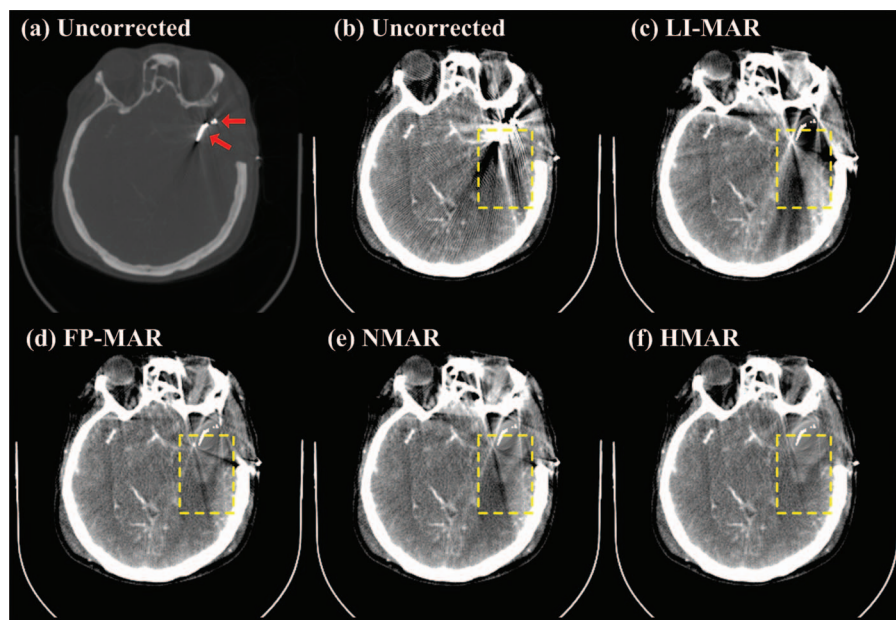
FIG. 13. The head CT images show patient 2 with a cerebral artery aneurysm after clipping surgery. (a) and (b) are the uncorrected images, the arrows in (a) point out the clip, and (c)–(f) the corrected results by LI-MAR, FP-MAR, NMAR, and HMAR, respectively. The window width and window level are (WW = 4000 HU, WL = 1000 HU) for (a) and (WW = 200 HU, WL = 50 HU) for (b)–(f), respectively.

greatly. Therefore, the profiles are smoother in the constrained HMAR prior than that in the other prior images, as shown in Figs. 11(f) and 11(g). Moreover, as shown in Fig. 11(e), CT number variance in soft tissues has been recovered to a large extent in the constrained HMAR prior image, which makes it closer to the ground truth.

Figure 12 shows some other head CT images of patient 1, in which there are three adjacent dental fillings in the upper jaw. It is clear that HMAR can obtain a better corrected image, reducing the dark streak artifacts indicated by arrow 1 more dramatically than the other three MAR methods. Besides, unlike the other three MAR methods,
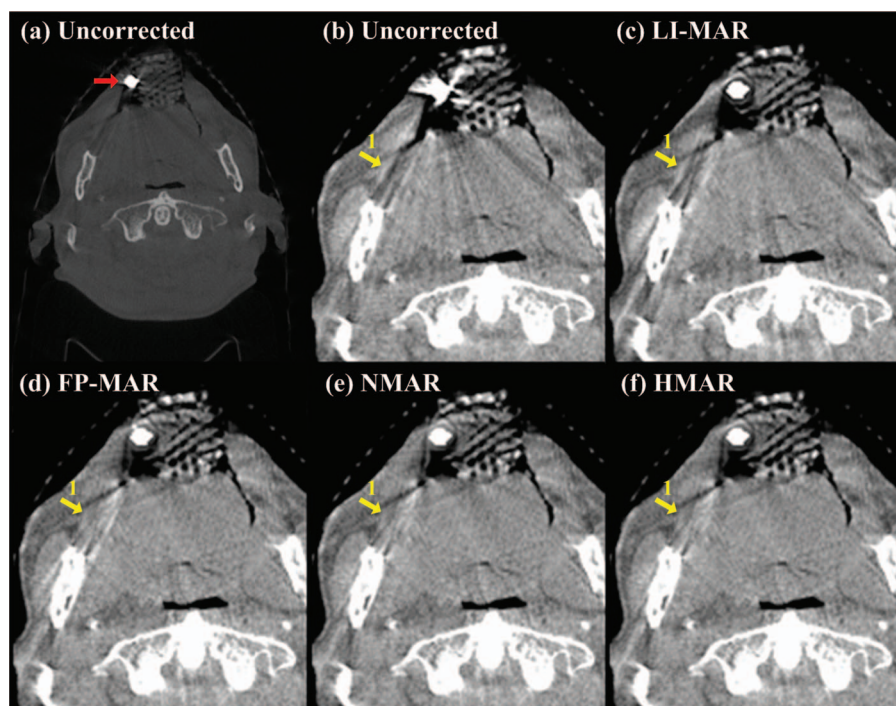

FIG. 14. Patient 3, slice through a single metal in head. (a) and (b) the uncorrected images, the arrow in (a) points out the metal, and (c)–(f) the corrected results by LI-MAR, FP-MAR, NMAR, and HMAR, respectively. (b)–(f) are the magnifications of partial images. The window width and window level are (WW = 4000 HU, WL = 1000 HU) for (a) and (WW = 750 HU, WL = 0 HU) for (b)–(f), respectively.
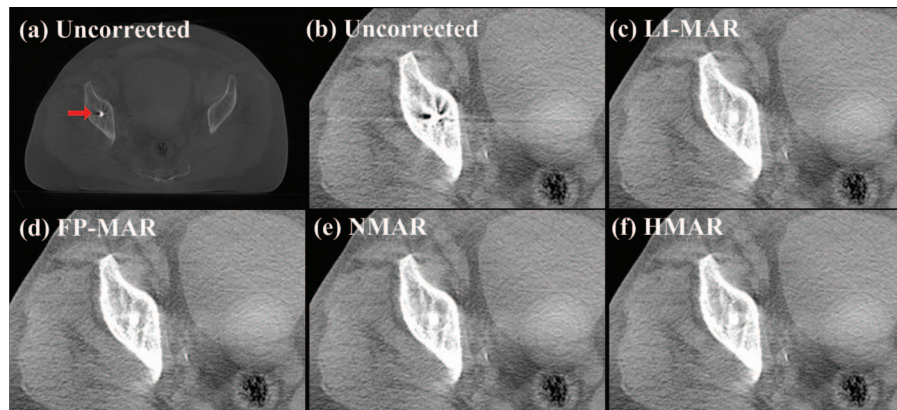
FIG. 15. Patient 4, slice through a fixation screw in the pelvis. (a) and (b) the uncorrected images, the arrow in (a) points out the screw, and (c)–(f) the corrected results by LI-MAR, FP-MAR, NMAR, and HMAR, respectively. (b)–(f) are the magnifications of partial images. The window width and window level are (WW = 4000 HU, WL = 1000 HU) for (a) and (WW = 750 HU, WL = 0 HU) for (b)–(f), respectively.

HMAR can prevent the false structures as indicated by arrow 2.

Patient 2 is a 59 year-old female with diffused subarachnoid hemorrhage in the basal cisterns and sylvian fissures.[50] Figures 13(a) and 13(b) show a metallic clip in the region of cerebral artery aneurysm in head CT images. The uncorrected and LI-MAR corrected images contained massive artifacts. FP-MAR and NMAR can alleviate artifacts to some extent and HMAR can remove artifacts better and enable visualization of tissues around the clip, as can be seen in Figs. 13(d)–13(f). As highlighted in the rectangular region in Fig. 13(f), the bright hemorrhage and the surrounding dark cerebral edema can be clearly observed. HMAR indicates a superior artifact removal effect and the ability for imaging diagnosis after clipping surgery.

Figure 14 shows head CT images of patient 3, in which there is a single small metal. It can be seen from Fig. 14(c) that LI-MAR has very limited ability to reduce streak artifacts and it even introduces new slight artifacts. In comparison, FP-MAR, NMAR, and HMAR methods can suppress metal artifacts dramatically, and the intensity of the remaining artifacts pointed by arrow 1 is similar, as shown in Figs. 14(d)–14(f). Since the remaining artifacts in LI-MAR corrected image are not severe, it is easy to get a good prior image even by using a simple thresholding technique (such as the tissue-class model). Therefore, all forward projection based MAR methods can achieve results with few artifacts.

Figure 15 shows pelvis CT images of patient 4, in which there is a metallic screw. It can be seen from Fig. 15 that all the four methods can remove metal artifacts almost completely. In this projection dataset, although there is still no prior information for LI-MAR, the projections around the metal trace are very flat, so linear interpolation is a good estimation of the missing projection caused by small metal.[21] With more prior information than LI-MAR, it is easy to obtain good results from the three prior image based MAR methods.

The above-mentioned five sets of CT slices were blind reviewed by two radiologists (Reviewers A and B). The five CT images in each set were displayed side by side in a random order, and the reviewers were allowed to zoom in and out and adjust window width and window level. Regarding the overall image quality and visual conspicuity of anatomic recognition, images in each set were ranked from 1 (the best image) to 5 (the worst image).[51] The ranking results are as shown in Table III. Uncorrected images are always regarded as the worst and all MAR methods have a positive effect on image quality. HMAR is ranked as the best for all patients' scans by both radiologists. The rank of NMAR is 2.1 on average, followed by FP-MAR and LI-MAR whose mean ranks are 3.1 and 3.2, respectively.

All MAR methods were implemented on an Intel(R) Core(TM) i7-2600 CPU, 3.40GHz with 4GB of RAM–PC platform, using MATLAB. Our code was not optimized for better speed and only one core of CPU was utilized to run the

TABLE III. Rank of image quality assigned by two radiologists.

	Patient 1 @lower jaw		Patient 1 @upper jaw		Patient 2		Patient 3		Patient 4		
	A	B	A	B	A	B	A	B	A	B	Mean
Uncorrected	5	5	5	5	5	5	5	5	5	5	5.0
LI-MAR	3	3	4	3	4	4	4	4	2	1	3.2
FP-MAR	4	4	3	4	2	2	3	3	2	4	3.1
NMAR	2	2	2	2	3	3	1	1	4	1	2.1
HMAR	1	1	1	1	1	1	1	1	1	1	1.0

code. Taking patients 1 and 3, for example, computation time of LI-MAR, FP-MAR, NMAR, and HMAR was 80s, 145s, 144s, and 299s, respectively, to obtain 512×512 corrected images from the 512 bins by 364 views raw data.

V. DISCUSSION AND CONCLUSION

Finding a good prior image is crucial in forward projection based methods. In our work, we find that the prior image being a "coarse" or "smooth" version of the ground truth may be a very good choice because it seizes both sides of the problem. One is that it has the streak artifacts removed, which avoids introduction of the artifacts; and the other is that it avoids the wrong tissues classification introduced by forcing unified intensity just as the competing methods do. Therefore, by using prior information of this "coarse" image, we can complete projection and simultaneously prevent bringing streak artifacts and false structures in the corrected image.

Some iterative MAR algorithms using incomplete projection, such as the TV based MAR methods[32,33] and the constrained optimization based MAR (Ref. 27) may achieve good results, but the key problem is how to strike a balance between image details and regularization. Parameters selection for the balance is based on the image content and the noise level. Thus, parameters are usually chosen empirically in each case. On the contrary, an over smoothed image is acceptable as a good prior image and thus the parameters and iteration stopping criteria in HMAR method are easy to set. Meanwhile, the proposed LUC component is efficient to deal with the severe ill-posed problem around metal. As a result, all parameters in HMAR method are fixed for every case in this study, which will benefit its applications.

The general goal is to promote the CT image quality and meanwhile, lower computational cost as much as possible. For MAR methods, CT image reconstruction and forward projection account for a dominant proportion of computational time. Both FP-MAR and NMAR need three conventional FBP reconstructions and two forward projections, while HMAR need two extra iterations for reconstruction. Although HMAR need more computational cost than FP-MAR and NMAR, it has better correction performance. In addition, HMAR needs fewer main iterations compared with other OS based accelerated iterative MAR algorithms, e.g., the MAR method in Ref. 20 needs seven main iterations in the MAP reconstruction procedure. In short, HMAR can find a good trade-off between image quality and computational efficiency.

Although the HMAR method is developed for 2D CT, it can also be applied to 3D cases slice by slice as demonstrated in the patients' experiments. Besides, since the number of patients is not sufficient, statistical analysis of ranking results is not carried out. In order to further validate the effectiveness of the proposed method, we will test HMAR on more patients' measurements and statistically analyze results in our future work.

In conclusion, this paper proposes a novel HMAR method based on forward projection. The key idea is to find a good prior image by the proposed TV iterative reconstruction with the local uniformity constraint around metals, and the itera-

tion is initialized with a precorrected image to save the computations. Then the raw projection is completed by the forward projection of the prior image. Experimental results show that the HMAR can reduce metal artifacts significantly and restore image information successfully, especially in the case of severe metal implants. In the future, we will focus on validating the HMAR method on more metallic implants cases.

ACKNOWLEDGMENTS

a)Author to whom correspondence should be addressed. Electronic mail: xqmou@mail.xjtu.edu.cn

[1] D. D. Robertson, P. J. Weiss, E. K. Fishman, D. Magid, and P. S. Walker, "Evaluation of CT techniques for reducing artifacts in the presence of metallic orthopedic implants," J. Comput. Assist. Tomogr. **12**, 236–241 (1988).

[2] M. L. Kataoka, M. G. Hochman, E. K. Rodriguez, P. J. P. Lin, S. Kubo, and V. D. Raptopolous, "A review of factors that affect artifact from metallic hardware on multi-row detector computed tomography," Curr. Probl Diagn. Radiol. **39**, 125–136 (2010).

[3] B. De Man, J. Nuyts, P. Dupont, G. Marchal, and P. Suetens, "Metal streak artifacts in x-ray computed tomography: A simulation study," IEEE Trans. Nucl. Sci. **46**, 691–696 (1999).

[4] B. De Man, J. Nuyts, P. Dupont, G. Marchal, and P. Suetens, "Reduction of metal streak artifacts in x-ray computed tomography using a transmission maximum a posteriori algorithm," IEEE Trans. Nucl. Sci. **47**, 977–981 (2000).

[5] B. De Man, J. Nuyts, P. Dupont, G. Marchal, and P. Suetens, "An iterative maximum-likelihood polychromatic algorithm for CT," IEEE Trans. Med. Imaging **20**, 999–1008 (2001).

[6] J. F. Williamson, B. R. Whiting, J. Benac, R. J. Murphy, G. J. Blaine, J. A. O'Sullivan, D. G. Politte, and D. L. Snyder, "Prospects for quantitative computed tomography imaging in the presence of foreign metal bodies using statistical image reconstruction," Med. Phys. **29**, 2404–2418 (2002).

[7] W. Kalender, R. Hebel, and J. Ebersberger, "Reduction of CT artifacts caused by metallic implants," Radiology **164**, 576–577 (1987).

[8] G. H. Glover and N. J. Pelc, "An algorithm for the reduction of metal clip artifacts in CT reconstructions," Med. Phys. **8**, 799–807 (1981).

[9] C. Xu, F. Verhaegen, D. Laurendeau, S. A. Enger, and L. Beaulieu, "An algorithm for efficient metal artifact reductions in permanent seed implants," Med. Phys. **38**, 47–56 (2011).

[10] A. H. Mahnken, R. Raupach, J. E. Wildberger, B. Jung, N. Heussen, T. G. Flohr, R. W. Gunther, and S. Schaller, "A new algorithm for metal artifact reduction in computed tomography: In vitro and in vivo evaluation after total hip replacement," Invest. Radiol. **38**, 769–775 (2003).

[11] J. Wei, L. Chen, G. A. Sandison, Y. Liang, and L. X. Xu, "X-ray CT high-density artefact suppression in the presence of bones," Phys. Med. Biol. **49**, 5407–5418 (2004).

[12] M. Oehler and T. Buzug, "Statistical image reconstruction for inconsistent CT projection data," Methods Inf. Med. **46**, 261–269 (2007).

[13] S. Y. Zhao, D. D. Roberston, G. Wang, B. Whiting, and K. T. Bae, "X-ray CT metal artifact reduction using wavelets: An application for imaging total hip prostheses," IEEE Trans. Med. Imaging **19**, 1238–1247 (2000).

[14]B. Kratz and T. M. Buzug, "Metal artifact reduction in computed tomography using nonequispaced Fourier transform," *Nuclear Science Symposium Conference Record (NSS/MIC)* (IEEE, Orlando, FL, 2009), pp. 2720–2723.

[15]Y. Zhang, L. Zhang, X. R. Zhu, A. K. Lee, M. Chambers, and L. Dong, "Reducing metal artifacts in cone-beam CT images by preprocessing projection data," Int. J. Radiat. Oncol., Biol., Phys. **67**, 924–932 (2007).

[16]W. J. H. Veldkamp, R. M. S. Joemai, A. J. van der Molen, and J. Geleijns, "Development and validation of segmentation and interpolation techniques in sinograms for metal artifact suppression in CT," Med. Phys. **37**, 620–628 (2010).

[17]J. Wu, C. T. Shih, S. J. Chang, T. C. Huang, J. Y. Sun, and T. H. Wu, "Metal artifact reduction algorithm based on model images and spatial information," Nucl. Instrum. Methods Phys. Res. A **652**, 602–605 (2011).

[18]D. Prell, Y. Kyriakou, M. Beister, and W. A. Kalender, "A novel forward projection-based metal artifact reduction method for flat-detector computed tomography," Phys. Med. Biol. **54**, 6575–6591 (2009).

[19]M. Bal and L. Spies, "Metal artifact reduction in CT using tissue-class modeling and adaptive prefiltering," Med. Phys. **33**, 2852–2859 (2006).

[20]C. Lemmens, D. Faul, and J. Nuyts, "Suppression of metal artifacts in CT using a reconstruction procedure that combines MAP and projection completion," IEEE Trans. Med. Imaging **28**, 250–260 (2009).

[21]E. Meyer, R. Raupach, M. Lell, B. Schmidt, and M. Kachelriess, "Normalized metal artifact reduction (NMAR) in computed tomography," Med. Phys. **37**, 5482–5493 (2010).

[22]C. S. Olive, M. R. Kaus, V. Pekar, K. Eck, and L. Spies, "Segmentation aided adaptive filtering for metal artifact reduction in radio-therapeutic CT images," Proc. SPIE **5370**, 1991–2002 (2004).

[23]G. Wang, M. W. Vannier, and P. C. Cheng, "Iterative x-ray cone-beam tomography for metal artifact reduction and local region reconstruction," Microsc. Microanal. **5**, 58–65 (1999).

[24]G. Wang, D. L. Snyder, J. A. OSullivan, and M. W. Vannier, "Iterative deblurring for CT metal artifact reduction," IEEE Trans. Med. Imaging **15**, 657–664 (1996).

[25]D. D. Robertson, J. Yuan, G. Wang, and M. W. Vannier, "Total hip prosthesis metal-artifact suppression using iterative deblurring reconstruction," J. Comput. Assist. Tomogr. **21**, 293–298 (1997).

[26]D. L. Snyder, J. A. O'Sullivan, R. J. Murphy, D. G. Politte, B. R. Whiting, and J. F. Williamson, "Image reconstruction for transmission tomography when projection data are incomplete," Phys. Med. Biol. **51**, 5603–5619 (2006).

[27]X. Zhang, J. Wang, and L. Xing, "Metal artifact reduction in x-ray computed tomography (CT) by constrained optimization," Med. Phys. **38**, 701–711 (2011).

[28]E. Y. Sidky, C. M. Kao, and X. H. Pan, "Accurate image reconstruction from few-views and limited-angle data in divergent-beam CT," J. X-Ray Sci. Technol. **14**, 119–139 (2006).

[29]E. Y. Sidky and X. C. Pan, "Image reconstruction in circular cone-beam computed tomography by constrained, total-variation minimization," Phys. Med. Biol. **53**, 4777–4807 (2008).

[30]H. Y. Yu and G. Wang, "Compressed sensing based interior tomography," Phys. Med. Biol. **54**, 2791–2805 (2009).

[31]L. Ritschl, F. Bergner, C. Fleischmann, and M. Kachelrieß, "Improved total variation-based CT image reconstruction applied to clinical data," Phys. Med. Biol. **56**, 1545–1561 (2011).

[32]Y. Zhang, X. Mou, and H. Yan, "Weighted total variation constrained reconstruction for reduction of metal artifact in CT," *Nuclear Science Symposium and Medical Imaging Conference (2010 NSS/MIC)* (IEEE, Knoxville, TN, 2010), pp. 2630–2634.

[33]X. Zhang, J. Wang, and L. Xing, "Metal artifact reduction in computed tomography by constrained optimization," *Proc. SPIE* **7622**, 76221T (2010).

[34]J. Choi, M. Kim, W. Seong, and J. Ye, "Compressed sensing metal artifact removal in dental CT," in *Proceedings of the Sixth IEEE International Conference on Symposium on Biomedical Imaging: From Nano to Macro* (IEEE, Boston, MA, 2009), pp. 334–337.

[35]M. Abdoli, R. A. J. O. Dierckx, and H. Zaidi, "Metal artifact reduction strategies for improved attenuation correction in hybrid PET/CT imaging," Med. Phys. **39**, 3343–3360 (2012).

[36]D. Xia, J. C. Roeske, L. Yu, C. A. Pelizzari, A. J. Mundt, and X. Pan, "A hybrid approach to reducing computed tomography metal artifacts in intracavitary brachytherapy," Brachytherapy **4**, 18–23 (2005).

[37]J. Choi, K. S. Kim, M. W. Kim, W. Seong, and J. C. Ye, "Sparsity driven metal part reconstruction for artifact removal in dental CT," J. X-Ray Sci. Technol. **19**, 457–475 (2011).

[38]F. E. Boas and D. Fleischmann, "Evaluation of two iterative techniques for reducing metal artifacts in computed tomography," Radiology **259**, 894–902 (2011).

[39]O. Watzke and W. A. Kalender, "A pragmatic approach to metal artifact reduction in CT: Merging of metal artifact reduced images," Eur. Radiology **14**, 849–856 (2004).

[40]S. Mazin and N. Pelc, "SU-EE-A4-03: Metal artifact reduction algorithm for x-ray CT using a three-pass approach," Med. Phys. **36**, 2432 (2009).

[41]G. Herman and L. Meyer, "Algebraic reconstruction techniques can be made computationally efficient," IEEE Trans. Med. Imaging **12**, 600–609 (1993).

[42]H. Erdogan and J. Fessler, "Ordered subsets algorithms for transmission tomography," Phys. Med. Biol **44**, 2835–2851 (1999).

[43]International Commission on Radiation Units and Measurements, "Tissue substitutes in radiation dosimetry and measurements," ICRU Report No. 44 (ICRU Publications, Washington, DC, 1989).

[44]M. J. Berger, J. H. Hubbell, S. M. Seltzer, J. Chang, J. S. Coursey, R. Sukumar, D. S. Zucker, and K. Olsen, "XCOM: Photon Cross Sections Database, NIST Standard Reference Database 8 (XGAM)," *The National Institute of Standards and Technology (NIST)*, Gaithersburg, MD, 2009, see http://www.nist.gov/pml/data/xcom/index.cfm.

[45]S. Tang, X. Mou, Y. Yang, Q. Xu, and H. Yu, "Application of projection simulation based on physical imaging model to the evaluation of beam hardening corrections in x-ray transmission tomography," J. X-Ray Sci. Technol. **16**, 95–117 (2008).

[46]F. Noo, M. Defrise, and R. Clackdoyle, "Single-slice rebinning method for helical cone-beam CT," Phys. Med. Biol. **44**, 561–570 (1999).

[47]S. Wesarg, M. Ebert, and T. Bortfeld, "Parker weights revisited," Med. Phys. **29**, 372–378 (2002).

[48]G. Wang, "X-ray micro-CT with a displaced detector array," Med. Phys. **29**, 1634–1636 (2002).

[49]E. Hansis, J. Bredno, D. Sowards-Emmerd, and S. Lingxiong, "Iterative reconstruction for circular cone-beam CT with an offset flat-panel detector," *Nuclear Science Symposium Conference Record (NSS/MIC)* (IEEE, Knoxville, TN, 2010), pp. 2228–2231.

[50]H. Y. Yu, K. Zeng, D. K. Bharkhada, G. Wang, M. T. Madsen, O. Saba, B. Policeni, M. A. Howard, and W. R. K. Smoker, "A segmentation-based method for metal artifact reduction," Acad. Radiol. **14**, 495–504 (2007).

[51]J. M. Verburg and J. Seco, "CT metal artifact reduction method correcting for beam hardening and missing projections," Phys. Med. Biol. **57**, 2803–2818 (2012).

[52]W. Zhuang, S. S. Gopal, and T. J. Hebert, "Numerical evaluation of methods for computing tomographic projections," IEEE Trans. Nucl. Sci. **41**, 1660–1665 (1994).